Nanoscale

PAPER

View Article Online
View Journal | View Issue

Cite this: *Nanoscale*, 2024, **16**, 14081

Doping-mediated excited state dynamics of diphosphine-protected M@Au_{12} (M = Au, Ir) superatom nanoclusters†

Wei Pei, *[a] Lei Hou,[a] Jing Yang,[a] Si Zhou*[b,c] and Jijun Zhao *[b,c]

Received 13th May 2024,
Accepted 29th June 2024

DOI: 10.1039/d4nr02051k

rsc.li/nanoscale

Doping heterometal atoms into ligand-protected gold superatom nanoclusters (Au_n NCs) is proposed to further diversify their geometrical and electronic structures and enhance their photoluminescence properties, which is attributed to the mixing and effects between atoms. However, the fundamental principles that govern the optoelectronic properties of the doped Au_n NCs remain elusive. Herein, we systematically explored two prototypical 8-electron Au_n (n = 11 and 13) NCs with and without Ir dopant atoms using comprehensive *ab initio* calculations and real-time nonadiabatic molecular dynamics simulations. These doped Au_n NCs maintain their parent geometrical structures and 8-electron superatomic configuration ($1S^2 1P^6$). Strong core–shell (Ir–Au_n) electronic coupling significantly expands the energy gap, resulting in a weak nonadiabatic coupling matrix element, which in turn increases the carrier lifetime. This increase is mainly governed by the low-frequency vibration mode. We uncovered the relationship between electronic structures, electron–vibration, and carrier dynamics for these doped Au_n NCs. These calculated results provide crucial insights for the atomically precise design of metal NCs with superior optoelectronic properties.

1. Introduction

Ligand-protected gold nanoclusters (Au NCs) hold immense promise as nanoscale functional materials owing to their size-specific physicochemical properties, which can be tailored by the manipulation of their composition, size, and ligands,[1,2] rendering them akin to atoms. This analogy extends to magic-sized Au NCs, prized for their atom-like characteristics, where metal atoms mimic nucleons and valence electrons imitate atomic electrons.[3–5] This unique behavior opens up diverse applications in luminescence, biomedicine, sensing, photonics, and photo-relative fields.[6,7] However, highly luminescent Au NCs remain rare, primarily due to nonradiative relaxation dominating the excited state, resulting in low photoluminescence (PL) quantum yields (<1%), presenting obstacles for practical applications. To address these challenges, several strategies have been explored,[8] including core etching and alloying,[9] capped-ligand engineering,[9] heteroatom doping, aggregation-induced emission (AIE), and surrounding medium.[10]

Among them, atomically precise doping-induced enhancement emerges as a standout strategy for fine-tuning the performance of ligand-protected Au NCs.[8,11,12] This approach not only enables the adjustment of the emission properties of Au NCs, but also provides valuable atomic-level insight into the origin of their emission. Through experimentation, Tsukuda *et al.* synthesized a series of diphosphine-protected M@Au_{12} (M = Pt, Ir, Ru, Rh, Pd) NCs with PL quantum yields of 46%–67%.[13] This dramatic enhancement of PL was attributed to the expansion of the energy gap by the upshifted 1P 8-electron (8e) superatomic orbitals,[14] which retarded the nonradiative decay of the photoexcited state by decoupling it from the excited state to the ground state, resulting in a longer excited-state lifetime.[15,16] Jin and Ramakrishna *et al.* demonstrated that thiolate-protected M@Au_{24} NCs [M@$Au_{24}(SR)_{18}$] with an 8e superatomic configuration possess a longer excited-state lifetime (50–200 ns) compared to the non-8e configuration of M@$Au_{24}(SR)_{18}$ (<5 ps).[17,18] This phenomenon was attributed to the introduction of heteroatoms, which triggered strong core–

[a]*College of Physical Science and Technology, Yangzhou University, Yangzhou 225009, China. E-mail: pwei@yzu.edu.cn*
[b]*Guangdong Basic Research Center of Excellence for Structure and Fundamental Interactions of Matter, Guangdong Provincial Key Laboratory of Quantum Engineering and Quantum Materials, School of Physics, South China Normal University, Guangzhou 510006, China. E-mail: sizhou@m.scnu.edu.cn, zhaojj@dlut.edu.cn*
[c]*Guangdong-Hong Kong Joint Laboratory of Quantum Matter, Frontier Research Institute for Physics, South China Normal University, Guangzhou 510006, China*

†Electronic supplementary information (ESI) available: Optical absorption spectrum and time evolution of the Kohn–Sham molecular orbital of ligand-protected Au NCs. See DOI: https://doi.org/10.1039/d4nr02051k

shell electron coupling, thereby regulating the distribution and configuration of the valence electron wave function to stabilize the excited state of ligand-protected Au NCs and determine their carrier dynamics behavior.[19] Existing experimental measurements to directly observe the relaxation of atoms, electrons and energy in the excited state dynamics of ligand-protected Au NCs remain challenging, hindering the elucidation of the origin of their emission.

Based on the time-dependent density functional theory (TD-DFT), the Aikens group conducted extensive theoretical investigations focusing on the thiolate-protected Au_{25} NCs and phosphine-protected Au_{13} NCs,[20,21] both exhibiting emissions originating from Au_{13} core-based transitions, *i.e.*, superatomic 1D → 1P transitions, regardless of different ligands. The tuning of these transition channels is achieved through dopant–Au_n cage interactions, which determine the degree of electron–hole overlap, thereby regulating emission energy and intensity for phosphine-protected $M@Au_{12}$ NCs. Additionally, *ab initio* real-time nonadiabatic molecular dynamics (NAMD) simulations provide a means to address complex photoexcited phenomena and reveal intricate photoinduced processes at the atomic level.[21–24] Recent research has demonstrated that the distinct excited-state behavior of $M@Au_{24}(SR)_{18}$ NCs is doubly modulated by the sp–d and d–d orbital hybridization strengths of M dopants and the Au_{13} core in radiative dynamics.[25] The configuration of Au_n core packing in $Au_n(SR)_m$ NCs plays a crucial role in tuning electron–phonon couplings, determining the lifetime of excited states.[26,27] Compared to thiolate ligands, understanding the mechanisms of the doping effect in phosphine-protected Au NCs remains elusive, as comprehensive calculations combining TD-DFT with NAMD have yet to establish an explicit correlation between the electronic structures and emission properties.

As prototypical phosphine-protected Au NCs, Au_{11} and Au_{13} NCs exhibit $1S^21P^6$ configurations based on the jellium model and serve as vital basic building blocks for forming larger or alloyed Au_n NCs. Herein, we systematically explored the geometrical, electronic, and absorption properties, and excited-state dynamics of Au_n NCs when the central Au atom is replaced by an Ir atom. The interfacial electronic coupling between dopant atoms and the Au_n cage plays a crucial role in renormalizing the Kohn–Sham orbital arrangement and tuning the dynamic behavior of photogenerated carriers. Through elucidating the relationship among the carrier lifetime, electronic structures, and electron–vibration coupling, we pave the way for the rational design of ligand-protected metal NCs with targeted optoelectronic properties.

2. Computational methods

All the ground states (S_0) and excited states (S_n, n is the number of excited states) were fully optimized using DFT and TD-DFT calculations, as employed in the Gaussian 09 software package.[28] According to our previous studies,[29] the LANL2DZ and 6-311+G(d) basis sets were used for metal and non-metal atoms, respectively. The optical absorption spectra involve at least 300 possible transition channels. The analysis of electronic structures including charge density distribution of the frontier orbital, transition channel, and natural orbital population was conducted using Multiwfn3.8,[30] and the results were visualized using Visual Molecular Dynamics (VMD) software.[31] The adaptive natural density partition (AdNDP) method was employed to reveal the multicenter chemical bonding patterns of the ligand-protected Au NCs.[32]

The excited-state dynamics of ligand-protected Au NCs was simulated with Hefei-NAMD implemented in the Vienna *ab initio* simulation package (VASP)[33,34] using a plane-wave basis set with an energy cutoff of 500 eV, projector augmented wave (PAW) potentials,[35] and the generalized gradient approximation parameterized by Perdew, Burke, and Ernzerhof (GGA-PBE) for the exchange–correlation functional.[36] The ligand-protected Au NCs were placed in a cubic supercell with a lattice constant of 30 Å and their Brillouin zone was sampled using a 1 × 1 × 1 uniform k-point grid.[37] We used a velocity rescaling algorithm to maintain the temperature of the system at around 300 K. After that, a 2 ps microcanonical *ab initio* MD trajectory was generated with a 1 fs time step. The NAMD results were obtained by averaging over 50 different initial configurations randomly selected from the MD trajectory based on the classical path approximation.

3. Results and discussion

3.1 Geometrical structures and orbital analysis

In the laboratory, atomically precise Au NCs with 8e superatomic configurations have been widely synthesized,[1,2,8,11,13,38,39] owing to their excellent stabilities and unique molecule-like electronic structures. We first examined the atomic structures of phosphine halide-protected Au_{11} and Au_{13} NCs, as the two prototypical 8e Au_n NCs. To simplify our models and improve computational efficiency, the –triphenylphosphine (–PPh_3) and –diphosphine (–dppe) ligands were replaced by –$P(CH_3)_3$ and –$PCH_2(CH_3)_2$ ligands, respectively. This ligand simplification strategy has been successfully employed to explore the evaluation of geometrical and electronic structures of ligand-protected Au_n NCs in the theoretical simulation.[39,40] As shown in Fig. 1A and B, the $[Au_{11}(PPh_3)_8Cl_2]^{1+}$ NCs were composed of an incomplete centered icosahedral Au_{11} core with C_{2v} symmetry with eight PPh_3 ligands and two chloride atoms, while Au_{13} NCs have a prefect icosahedral Au_{13} core with D_5 symmetry protected by five dppe ligands and two chloride atoms. For the ligand-protected Au–alloy NCs, the center Au atoms were substituted with an Ir atom, possessing reversible redox characteristics between the 1^+ and 2^+ charge states[15] to regulate the electron configuration. Overall, the Ir-doped Au_n (n = 10 and 12) NCs maintain their parent configuration well with an average bond length between the Ir atoms and the Au atoms of 2.65–2.79 Å, indicating typical covalent bond interactions.[29] Consequently, the $Ir@Au_{10}$ and $Ir@Au_{12}$ cores exhibit higher symmetry, corresponding to D_{4d} and I_h, respectively, compared

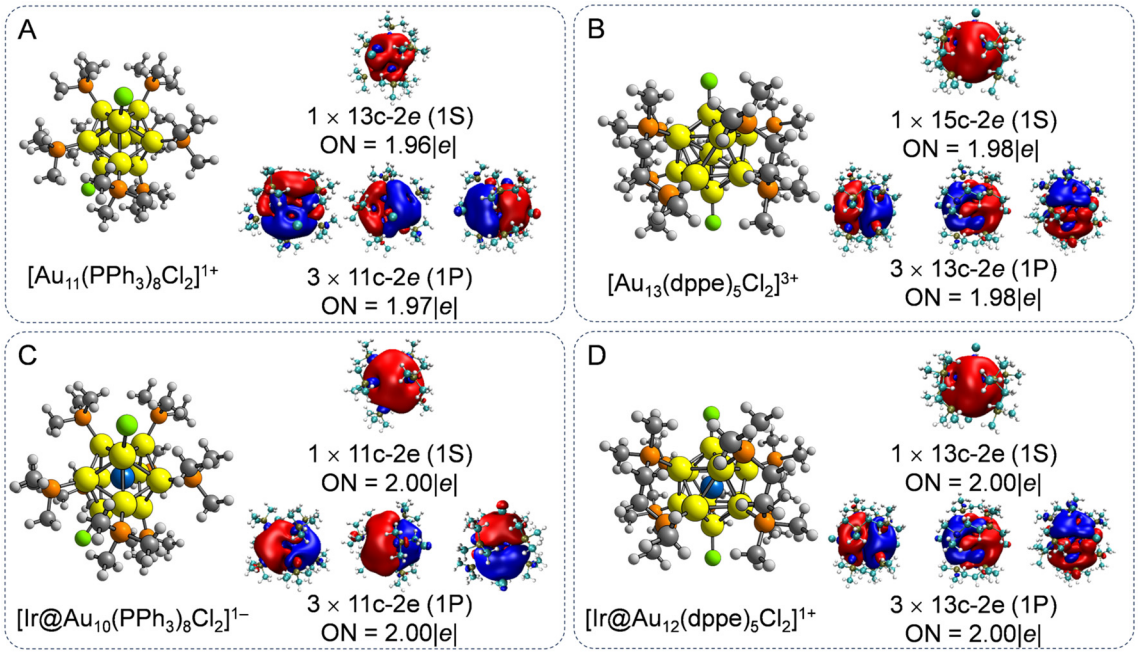

Fig. 1 Geometrical structures and AdNDP localized natural bonding orbitals of (A) $[Au_{11}(PPh_3)_8Cl_2]^{1+}$, (B)$[Au_{13}(dppe)_5Cl_2]^{3+}$, (C) $[Ir@Au_{10}(PPh_3)_8Cl_2]^{1-}$, and (D) $[Ir@Au_{12}(dppe)_5Cl_2]^{1+}$. ON is the occupation number.

to the C_{2v} and D_5 symmetries of undoped Au_{11} and Au_{13} NCs (Fig. 1C and D).

To deeply understand the chemical bonding interaction of ligand-protected Au NCs with and without Ir dopant atoms, AdNDP analysis was employed to describe multicenter bonding interactions, as shown in Fig. 1. The AdNDP analysis reveals four 11c–2e and 13c–2e σ-aromatic islands in both the doped and undoped Au_{11} and Au_{13} NCs, respectively, consistent with the 8e count fulfilling a $1S^21P^6$ electronic shell structure based on the empirical sphere jellium model.[41] The aromatic character of these ligand-protected Au NCs originates from the $[Au_{11}]^{3+}$, $[Ir@Au_{10}]^{1+}$, $[Au_{13}]^{5+}$, and $[Ir@Au_{12}]^{3+}$ cores, further revealing the enhanced stability of Au_{13}-based NCs.[42] This multicenter –2e binding pattern is in accordance with previous experimentally systemized $[Au_{19}(Hdppa)_3(C{\equiv}CPh)_9]^{2+}$,[43] $[Au_{25}(SR)_{18}]^-$,[44] $Au_{13}Cu_4(PPh_2Py)_3(SePh)_9$,[45] and $[Au_{13}Cu_2(PPh_3)_6(SR)_6]^+$.[46]

3.2 Absorption spectrum and electronic structures

Fig. 2 and S1† illustrate the computed optical absorption spectrum of ligand-protected Au_n NCs based on the TD-DFT framework. The undoped Au_{11} NCs exhibit three prominent peaks at 344 nm, 419 nm, and 477 nm, corresponding to excitation energies of 3.60 eV, 2.96 eV, and 2.60 eV, respectively, consistent with the experimental measurements at 312 nm, 416 nm, and 500 nm.[47] According to the transition contribution map, these characteristic peaks of Au_{11} NCs originate from some discrete excitation states, *i.e.* HOMO−2 → LUMO (peak a at 477 nm), HOMO−6 → LUMO, HOMO−5 → LUMO+1, and HOMO−4 → LUMO+2 (peak b at 419 nm), and HOMO−9 → LUMO+4, HOMO−3 → LUMO+5, and HOMO−2 → LUMO+8 (peak a at 317 nm). In the Kohn–Sham orbital energy level diagram of ligand-protected Au_{11} NCs, the molecular orbitals involved in these transitions are mainly composed of 6s5p and $5d^{10}$ atomic orbitals.[48] The absorption spectrum of $[Au_{13}(dppe)_5Cl_2]^{3+}$ NCs consists of prominent absorption peaks at 322 and 387 nm and a shoulder peak at 594 nm, in line with the experimental spectrum of the characteristic peaks of 300 nm, 390 nm, and 560 nm.[21] The prominent and shoulder peaks belong to the HOMO−2 → LUMO+7 and HOMO → LUMO+9, respectively, mainly originating from the atomic orbitals of the Au_{13} core, regardless of ligand atoms. This explains why ligand simplification can be used to describe the light absorption properties of such clusters. According to the sphere jellium model, it is found that superatomic P → D and P → F transitions mainly contribute to the prominent and shoulder absorption peaks of ligand-protected Au_n (n = 11 and 13) NCs (Fig. S1†).

Replacing the central Au atom with an Ir atom leads to a modification of the jellium potential, resulting in an increased energy gap of $Ir@Au_n$ (n = 10 and 12) NCs to 2.16–2.26 eV compared to their parent NCs of 1.86–1.93 eV. This increase can be contributed to the Ir dopant atoms, which have a low electronegativity (~2.2) and acquire electrons from the Au_n cage, causing an upshift in the HOMO and LUMO levels. Moreover, the increase in the LUMO level is significantly greater than that of the HOMO level upon doping with Ir atoms, yielding wider HOMO–LUMO gaps. As shown in Fig. 2A and B, the first absorption peak of $Ir@Au_n$ (n = 10 and 12) NCs experiences an obvious blueshift to 498 nm and 566 nm from 530 nm and

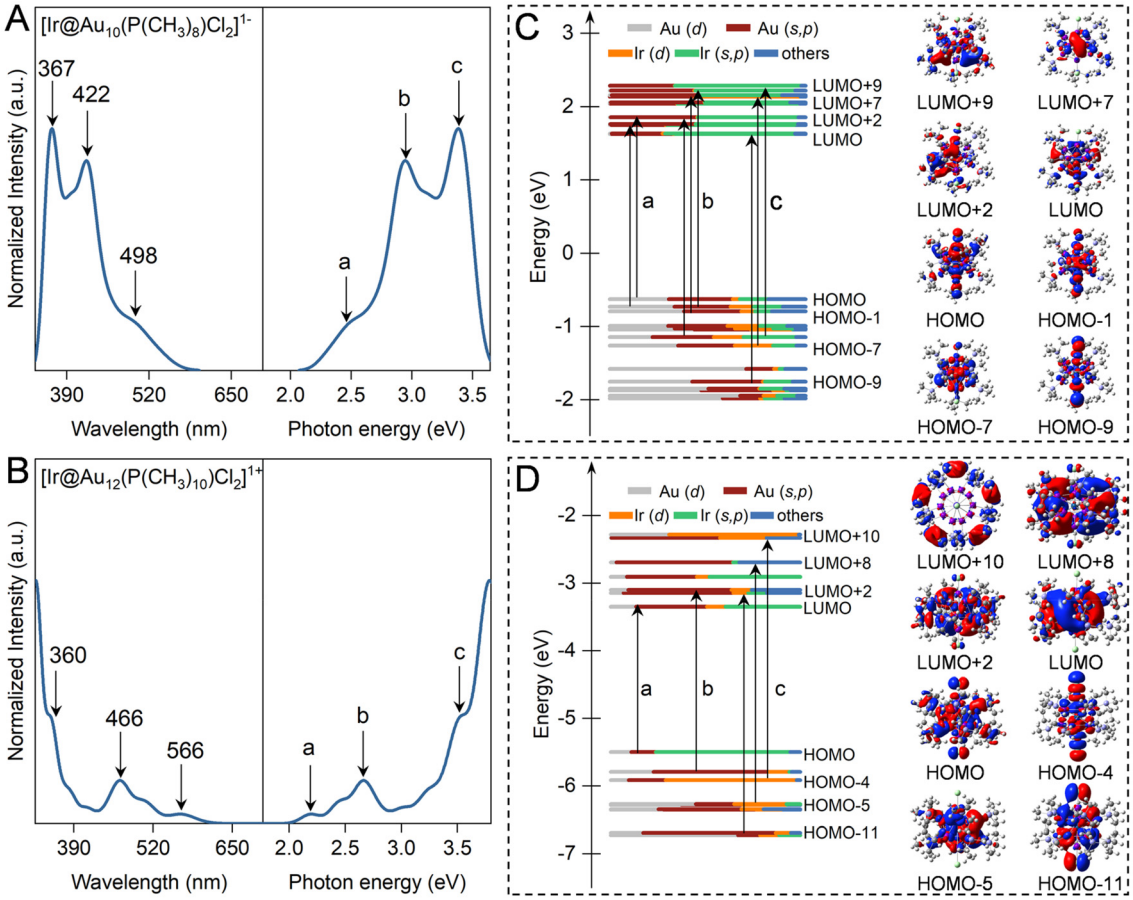

Fig. 2 (A and B) Optical absorption spectra and (C and D) the components of the Kohn–Sham molecular orbital of $[Ir@Au_{10}(PPh_3)_8Cl_2]^{1-}$ and $[Ir@Au_{12}(dppe)_5Cl_2]^{1+}$ NCs. The alphabets and numbers are the first three excited states. The red and blue colors denote the positive and negative phases of the wavefunction for selected molecular orbitals, respectively. The isosurface value is ± 0.02 a.u.

594 nm for the undoped Au_n (n = 11 and 13) NCs, respectively. The unoccupied d-orbital of Ir induces a strong core–shell interaction, leading to denser Kohn–Sham molecular orbitals near the front orbitals. This density allows for multiple excitations between many electronic states, resulting in broader absorption peaks. The unoccupied orbitals of $[Ir@Au_{10}(PPh_3)_8Cl_2]^{1-}$ NCs are composed of 6s5p orbitals of Ir and Au atoms, while the occupied ones are mixed composites with 5d and 6s5p of Ir and Au atoms. The contributions to the three strong absorption peaks of ligand-protected $Ir@Au_{10}$ NCs come from electronic transitions between the $5d^{10}$ atomic orbitals of the Au_{10} cage and the 6s5p orbital of Ir atoms, involving a typical core–shell transition behavior (Fig. 2C). In contrast, the HOMOs of $[Ir@Au_{12}(dppe)_5Cl_2]^{1+}$ NCs are mainly composed of the 6s5p orbital of Ir atoms (Fig. 2D), which are excited to the Au_{12} cage and its d orbital to participate in electronic transitions. Therefore, heteroatom doping can redistribute the electronic charge within the nanocluster, influencing both radiative and non-radiative recombination processes. This redistribution can significantly affect the photoluminescence properties of the material, either enhancing or quenching it, depending on the nature of the dopant atoms and their positions within the cluster.

3.3 Excited state dynamics behavior

According to the experimental femtosecond transient absorption spectrum of ligand-protected Au NCs,[49–51] the hot electrons in the high energy (HE)-excited states are first relaxed to the low-energy (LE) excited states and then to the position of the LUMO *via* a strong internal conversion, both of which are nonradiative processes. Subsequently, the electron in the LUMO experiences a weaker decay process to recombine with the hole in the HOMO, involving radiative transition, thereby yielding luminescence. To identify the key states involved in the dynamics and quantify the timescale of various processes, the HE and LE states for our ligand-protected Au NCs are presented as blue and orange lines in Fig. 3A and B, respectively, according to the orbital transition map of optical absorption combined with the orbital delocalization index. Therefore, we chose positions higher than LUMO ~ 1.00 eV and ~0.50 eV as the initial states of high- and low-excited states for hot electron relaxation, respectively. It should be noted that there are HE and LE states showing superatomic F and D characteristics, respectively, akin to typical superatomic fullerene clusters.[52] The LUMO and HOMO constitute the initial and final states

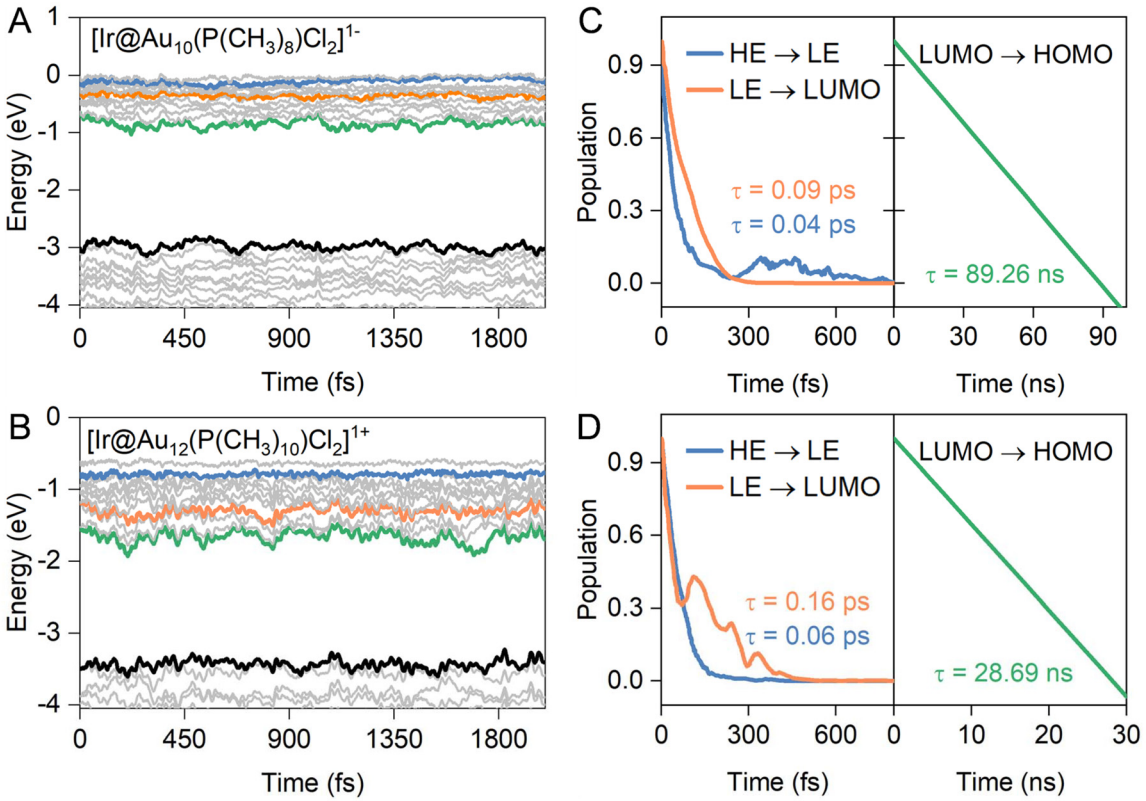

Fig. 3 Time evolution of the Kohn–Sham molecular orbital of (A) $[Ir@Au_{10}(PPh_3)_8Cl_2]^{1-}$ and (B) $[Ir@Au_{12}(dppe)_5Cl_2]^{1+}$ NCs. The colored solid lines represent the high-energy excited states (HE, blue), low-energy excited states (LE, orange), the lowest unoccupied molecular orbital (LUMO, green) and the highest occupied molecular orbital (HOMO, black) for each ligand-protected Au NC, respectively. Population evolution of the initial states of (C) $[Ir@Au_{10}(PPh_3)_8Cl_2]^{1-}$ and (D) $[Ir@Au_{12}(dppe)_5Cl_2]^{1+}$ NCs during the hot electron relaxation process, corresponding to their lifetimes indicated by colored Arabic numerals.

for the electron–hole (e–h) recombination across the energy gap for ligand-protected Au NCs. It is noteworthy that hot electron transitions between the HE and LE states, as well as between the LE and LUMO states, have a narrower energy gap, for which the fewest-switches surface-hopping (FSSH) method was employed.[53] However, the e–h recombination experiences a wider energy gap within a range from 1.77 eV to 2.36 eV. Quantum decoherence significantly influences this dynamic process, and thus, the decoherence-induced surface hopping (DISH) method was selected for simulations.[54]

Indeed, electron–phonon (e–p) interactions at finite temperature can exert a significant influence on the electronic structures of a system.[55,56] Fig. 3 and S2† depict the time-dependent evolution of the frontier orbitals for both undoped and doped ligand-protected Au_{11} and Au_{13} NCs calculated from *ab initio* molecular dynamics (AIMD) simulations within a micro-canonical ensemble for 2000 fs at 300 K. As a result, the high-energy excited state exhibits lower pronounced time-dependent oscillations, involving smaller vibration amplitudes within a range of 0.13–0.25 eV than that of the other three frontier orbitals (0.33–0.48 eV for LE, 0.38–0.56 eV for the LUMO, and 0.33–0.48 eV for the HOMO), irrespective of the presence of dopant atoms. The distinct e–p coupling-induced orbital renormalization is associated with the dynamics behavior of hot electrons in both carrier relaxation and recombination.[26,56] As shown in Fig. S2C and S2D,† the excited electrons of high-energy states relax to LE states (HE → LE) within the range of 1.23–3.64 ps for the undoped ligand-protected Au NCs, slightly longer than that of the Ir-doped systems (0.09–0.16 ps in Fig. 3C and D). Similarly, the LE → LUMO process exhibits fast electron relaxation behavior, with short timescales of 0.04–0.06 ps and 0.21–1.31 ps for the doped and undoped Au NCs, respectively. This discrepancy may be attributed to the heteroatom-induced denser arrangement of energy levels, resulting in lower nonadiabatic coupling elements between the initial states and the final states of electron transitions (more on this later).

In contrast to the aforementioned processes, the presence of an Ir dopant significantly suppresses the e–h recombination, leading to a prolonged carrier lifetime (τ). The carrier lifetime of ligand-protected $Ir@Au_{12}$ NCs is approximately ~29 ns, nearly three times longer than that of Au_{13} NCs at ~10 ns, consistent with experimental measurements where the photoluminescence lifetime of $Ir@Au_{12}$ is reported to be 2–3 times higher than that of Au_{13}.[16] This trend is further highlighted by the calculated e–h recombination of ~89 ns for $Ir@Au_{10}$ NCs, showing the slowest decay time constant, much higher than that of undoped Au_{11} NCs at τ = ~22 ns. These phosphine-pro-

Table 1 Average energy gap (ΔE), nonadiabatic coupling (NAC) elements, and the timescale of hot electron relaxation between the donor states and the acceptor states in the ligand-protected Au_n NCs

	HE → LE			LE → LUMO			LUMO → HOMO		
System	ΔE (eV)	NAC (meV)	Time (ps)	ΔE (eV)	NAC (meV)	Time (ps)	ΔE (eV)	NAC (meV)	Time (ns)
Au_{11}	0.57	2.68	1.23	0.62	6.05	0.21	1.86	0.57	22.33
$Ir@Au_{10}$	0.17	8.45	0.09	0.36	3.74	0.04	2.36	0.45	89.26
Au_{13}	1.18	1.98	3.64	0.71	2.14	1.31	1.77	0.71	10.21
$Ir@Au_{12}$	0.41	4.29	0.16	0.34	4.37	0.06	1.96	0.52	28.69

tected Au NCs possess longer carrier lifetimes compared to those of thiolate-protected Au NCs $[M@Au_{24}(SR)_{18}]^-$ (M = Pd, Pt, Cd, Hg) of 0.1–8 ns based on the DISH method.[25] In general, the lifetime of e–h recombination follows the sequence: $Ir@Au_{10} > Ir@Au_{12} > Au_{11} > Au_{13}$. The overall trend of carrier lifetimes observed in the four NCs is in line with previous experimental reports based on the time-resolved photoluminescence decay of ligand-protected Au NCs.[16,38] However, it is worth noting that the difference in carrier lifetimes between the NCs in our simulations is not as pronounced as observed in experimental studies. This discrepancy could be attributed to the experimental use of crystal structures of gold NCs, which introduces additional factors influencing carrier dynamics, including inter-cluster interactions and overall lattice symmetry.[26,27]

In previous theoretical studies based on NAMD simulations, the probability of hot electron relaxation is found to be sensitive to the nonadiabatic coupling (NAC) elements between the acceptor and donor states, which is defined as[34,57]

$$d_{jk} = \left\langle \varphi_j \left| \frac{\partial}{\partial t} \right| \varphi_k \right\rangle = \frac{\left\langle \varphi_j | \nabla_R H | \varphi_k \right\rangle}{\varepsilon_k - \varepsilon_j} \dot{R} \quad (1)$$

where $\langle \varphi_j | \nabla_R H | \varphi_k \rangle$ and ε_k–ε_j are the electron–phonon coupling strength and the energy gap between the Kohn–Sham orbitals of numbers j and k, respectively; $\dot{R}$ corresponds to nuclear velocity. Generally, a narrower energy gap and stronger e–p coupling lead to a larger NAC element, resulting in faster hot electron transition from the donor level to the acceptor level. Table 1 summarizes the average values of energy gap, NAC elements, and hot electron relaxation lifetimes of ligand-protected Au_n NCs with and without Ir dopants for the three electron transition channels mentioned above. In both the processes of HE → LE and LE → LUMO, the NAC strength is enhanced upon Ir doping, corresponding to the range of 3.74–8.45 meV with regard to the undoped system in the range of 2.14–6.05 meV. This enhancement in inelastic electron–vibrational scattering leads to faster electron transitions for $Ir@Au_n$ (n = 10 and 12) NCs.[58] The strong core–shell (Ir–Au_{10} and Ir–Au_{12}) electronic coupling significantly increases the HOMO–LUMO gap,[29] which results in weaker NAC elements (0.45–0.52 meV), suppressing the e–h recombination. We further explored the phonon excitations and e–p coupling *via* the Fourier transform of the autocorrelation functions of the HOMO–LUMO gap fluctuations (Fig. 4A). Except for the

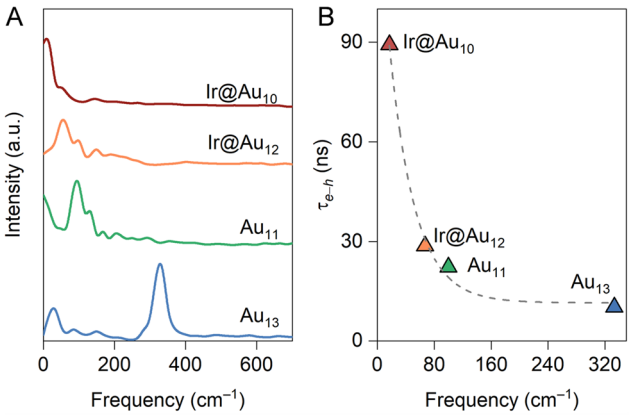

Fig. 4 (A) Fourier transforms of the autocorrelation functions of energy gap fluctuations for $[Au_{11}(PPh_3)_8Cl_2]^{1+}$, $[Ir@Au_{10}(PPh_3)_8Cl_2]^{1-}$, $[Au_{13}(dppe)_5Cl_2]^{3+}$, and $[Ir@Au_{12}(dppe)_5Cl_2]^{1+}$ NCs. (B) The lifetime between electrons and holes as a function of phonon modes for the above four Au_n NCs.

undoped Au_{13} NCs, the dominant phonon modes are low-frequency vibrational modes within a range of 0–200 cm^{-1}, which can be assigned to the bending, stretching, and liberation modes of the Au_n core unit.[59] The Au_{13} NCs show an intermediate frequency vibrational mode of ~333 cm^{-1}, corresponding to the normal modes of Au–Cl and Au–P bonds.[60] The low-frequency phonon modes are associated with the heavy atoms characterized by small nuclear velocities and weak electron–phonon interactions, resulting in a small NAC matrix element and a long carrier lifetime (Fig. 4B). These results suggest that the dopant-induced enhancement of the carrier lifetime of ligand-protected Au NCs can be attributed to both a stronger core–shell interaction resulting in a larger energy gap and tunable electron–vibration coupling determining the coupling of the frontier orbital.

4. Conclusion

In summary, we systematically explored the excited state dynamics of two prototypical 8e Au_n NCs (n = 11 and 13) with and without Ir dopant atoms using first-principles calculations combined with NAMD simulations. Owing to the strong core–shell (Ir–Au_n) electronic coupling, the HOMO–LUMO gap of the doped Au_n NCs was significantly increased, leading to an

obvious blueshift in their absorption spectrum compared to that of pristine systems. The high-energy excited state possesses low pronounced time-dependent oscillation, having fast hot electron relaxation regardless of the presence of dopant atoms. In e–h recombination, Ir dopant atoms induced an obvious inhibiting effect, which was governed by both the value of the energy gap and the peak of low-frequency phonon modes between the LUMO and the HOMO. This systematic study provides a practically useful guide to tuning the electronic structures and phonon modes to regulate the excited-state dynamic behavior of ligand-protected Au NCs by heteroatom doping.

Data availability

The data supporting the findings of this study are available within the article and its ESI.† Additional data that support the findings of this study are available from the corresponding author upon reasonable request.

Conflicts of interest

There are no conflicts of interest to declare.

Acknowledgements

This work was financially supported by the National Natural Science Foundation of China (12304300 and 12222403), the Natural Science Foundation of Jiangsu Province (No. BK20230555), the Natural Science Foundation of Jiangsu Higher Education Institutions of China (No. 23KJB140019), and the Outstanding Doctor Program of Yangzhou City 'Lv Yang Jin Feng' (No. YZLYJFJH2022YXBSO84).

References

1 M. R. Narouz, K. M. Osten, P. J. Unsworth, R. W. Y. Man, K. Salorinne, S. Takano, R. Tomihara, S. Kaappa, S. Malola, C.-T. Dinh, J. D. Padmos, K. Ayoo, P. J. Garrett, M. Nambo, J. H. Horton, E. H. Sargent, H. Häkkinen, T. Tsukuda and C. M. Crudden, *Nat. Chem.*, 2019, **11**, 419–425.
2 H. Hirai, S. Takano, T. Nakamura and T. Tsukuda, *Inorg. Chem.*, 2020, **59**, 17889–17895.
3 Z. Luo and A. W. Castleman, *Acc. Chem. Res.*, 2014, **47**, 2931–2940.
4 Z. Luo and S. Lin, *Coord. Chem. Rev.*, 2024, **500**, 215505.
5 B. D. Peter, W. Pei, G. N. Andrew, S. Zhou and Z. Luo, *Nanoscale*, 2024, **16**, 8090–8095.
6 L. Liu, P. Li, L.-F. Yuan, L. Cheng and J. Yang, *Nanoscale*, 2016, **8**, 12787–12792.
7 D.-e. Jiang and S. Dai, *Inorg. Chem.*, 2009, **48**, 2720–2722.
8 X. Kang and M. Zhu, *Chem. Soc. Rev.*, 2019, **48**, 2422–2457.
9 H.-H. Deng, X.-Q. Shi, F.-F. Wang, H.-P. Peng, A.-L. Liu, X.-H. Xia and W. Chen, *Chem. Mater.*, 2017, **29**, 1362–1369.
10 L.-Y. Chen, C.-W. Wang, Z. Yuan and H.-T. Chang, *Anal. Chem.*, 2015, **87**, 216–229.
11 H. Qian, M. Zhu, Z. Wu and R. Jin, *Acc. Chem. Res.*, 2012, **45**, 1470–1479.
12 M. Ebina, T. Iwasa, Y. Harabuchi and T. Taketsugu, *J. Phys. Chem. C*, 2018, **122**, 4097–4104.
13 H. Hirai, S. Takano, T. Nakashima, T. Iwasa, T. Taketsugu and T. Tsukuda, *Angew. Chem., Int. Ed.*, 2022, **61**, e202207290.
14 S. Takano, H. Hirai, T. Nakashima, T. Iwasa, T. Taketsugu and T. Tsukuda, *J. Am. Chem. Soc.*, 2021, **143**, 10560–10564.
15 H. Hirai, S. Takano, T. Nakamura and T. Tsukuda, *Inorg. Chem.*, 2020, **59**, 17889–17895.
16 H. Hirai, T. Nakashima, S. Takano, Y. Shichibu, K. Konishi, T. Kawai and T. Tsukuda, *J. Mater. Chem. C*, 2023, **11**, 3095–3100.
17 M. Zhou, C. Yao, M. Y. Sfeir, T. Higaki, Z. Wu and R. Jin, *J. Phys. Chem. C*, 2018, **122**, 13435–13442.
18 V. D. Thanthirige, M. Kim, W. Choi, K. Kwak, D. Lee and G. Ramakrishna, *J. Phys. Chem. C*, 2016, **120**(40), 23180–23188.
19 S. Maity, S. Kolay, S. Ghosh, S. Chakraborty, D. Bain and A. Patra, *J. Phys. Chem. Lett.*, 2022, **13**, 5581–5588.
20 R. D. Senanayake, A. V. Akimov and C. M. Aikens, *J. Phys. Chem. C*, 2017, **121**, 10653–10662.
21 K. L. D. M. Weerawardene, P. Pandeya, M. Zhou, Y. Chen, R. Jin and C. M. Aikens, *J. Am. Chem. Soc.*, 2019, **141**, 18715–18726.
22 K. L. D. M. Weerawardene, E. B. Guidez and C. M. Aikens, *J. Phys. Chem. C*, 2017, **121**, 15416–15423.
23 K. L. D. M. Weerawardene and C. M. Aikens, *J. Phys. Chem. C*, 2018, **122**, 2440–2447.
24 R. D. Senanayake, E. B. Guidez, A. J. Neukirch, O. V. Prezhdo and C. M. Aikens, *J. Phys. Chem. C*, 2018, **122**, 16380–16388.
25 X. Yu, Y. Sun, W.-w. Xu, J. Fan, J. Gao, X. Jiang, Y. Su and J. Zhao, *Nanoscale Horiz.*, 2022, **7**, 1192–1200.
26 X. Yu, W. Pei, W.-w. Xu, Y. Zhao, Y. Su and J. Zhao, *Inorg. Chem.*, 2023, **62**, 20450–20457.
27 X. Yu, Y. Su, W.-w. Xu and J. Zhao, *J. Phys. Chem. Lett.*, 2021, **12**, 2312–2319.
28 M. J. Frisch, G. W. Trucks, H. B. Schlegel, G. E. Scuseria, M. Robb, J. R. Cheeseman, G. Scalmani, V. Barone, B. Mennucci and G. A. Petersson, Wallingford Ct, 2009, vol. **2009**.
29 J. She, W. Pei, S. Zhou and J. Zhao, *J. Phys. Chem. Lett.*, 2022, **13**, 5873–5880.
30 T. Lu and F. Chen, *J. Comput. Chem.*, 2012, **33**, 580–592.
31 W. Humphrey, A. Dalke and K. Schulten, *J. Mol. Graphics*, 1996, **14**, 33–38.
32 D. Y. Zubarev and A. I. Boldyrev, *Phys. Chem. Chem. Phys.*, 2008, **10**, 5207–5217.
33 G. Kresse and J. Furthmüller, *Phys. Rev. B: Condens. Matter Mater. Phys.*, 1996, **54**, 11169–11186.

34 Q. Zheng, W. Chu, C. Zhao, L. Zhang, H. Guo, Y. Wang, X. Jiang and J. Zhao, *Wiley Interdiscip. Rev.: Comput. Mol. Sci.*, 2019, **9**, e1411.
35 G. Kresse and D. Joubert, *Phys. Rev. B: Condens. Matter Mater. Phys.*, 1999, **59**, 1758–1775.
36 J. P. Perdew, K. Burke and M. Ernzerhof, *Phys. Rev. Lett.*, 1996, **77**, 3865–3868.
37 H. J. Monkhorst and J. D. Pack, *Phys. Rev. B: Solid State*, 1976, **13**, 5188–5192.
38 X.-J. Zhai, J.-H. Hu, J. Guan, Y. Si, X.-Y. Dong, P. Luo, F. Pan, Z. Yu, R. Han and S.-Q. Zang, *Nano Res.*, 2023, **16**, 11366–11374.
39 D. Yang, W. Pei, S. Zhou, J. Zhao, W. Ding and Y. Zhu, *Angew. Chem., Int. Ed.*, 2020, **59**, 1919–1924.
40 S. Zhao, N. Austin, M. Li, Y. Song, S. D. House, S. Bernhard, J. C. Yang, G. Mpourmpakis and R. Jin, *ACS Catal.*, 2018, **8**, 4996–5001.
41 S. B. Zhang, M. L. Cohen and M. Y. Chou, *Phys. Rev. B: Condens. Matter Mater. Phys.*, 1987, **36**, 3455–3458.
42 N. Fedik, A. I. Boldyrev and A. Muñoz-Castro, *Phys. Chem. Chem. Phys.*, 2019, **21**, 25215–25219.
43 X.-K. Wan, Q. Tang, S.-F. Yuan, D.-e. Jiang and Q.-M. Wang, *J. Am. Chem. Soc.*, 2015, **137**, 652–655.
44 J. J. Li, Z. J. Guan, Z. Lei, F. Hu and Q. M. Wang, *Angew. Chem.*, 2019, **131**, 1095–1099.
45 Y. Song, Y. Lv, M. Zhou, T.-Y. Luo, S. Zhao, N. L. Rosi, H. Yu, M. Zhu and R. Jin, *Nanoscale*, 2018, **10**, 12093–12099.
46 H. Yang, Y. Wang, J. Lei, L. Shi, X. Wu, V. Mäkinen, S. Lin, Z. Tang, J. He and H. Häkkinen, *J. Am. Chem. Soc.*, 2013, **135**, 9568–9571.
47 L. C. McKenzie, T. O. Zaikova and J. E. Hutchison, *J. Am. Chem. Soc.*, 2014, **136**, 13426–13435.
48 M. Zhu, C. M. Aikens, F. J. Hollander, G. C. Schatz and R. Jin, *J. Am. Chem. Soc.*, 2008, **130**, 5883–5885.
49 W. Zhang, J. Kong, Y. Li, Z. Kuang, H. Wang and M. Zhou, *Chem. Sci.*, 2022, **13**, 8124–8130.
50 M. Zhou, C. Zeng, M. Y. Sfeir, M. Cotlet, K. Iida, K. Nobusada and R. Jin, *J. Phys. Chem. Lett.*, 2017, **8**, 4023–4030.
51 Q. Li, M. Zhou, W. Y. So, J. Huang, M. Li, D. R. Kauffman, M. Cotlet, T. Higaki, L. A. Peteanu and Z. Shao, *J. Am. Chem. Soc.*, 2019, **141**, 5314–5325.
52 H. Guo, C. Zhao, Q. Zheng, Z. Lan, O. V. Prezhdo, W. A. Saidi and J. Zhao, *J. Phys. Chem. Lett.*, 2018, **9**, 3485–3490.
53 J. C. Tully, *J. Chem. Phys.*, 1990, **93**, 1061–1071.
54 H. M. Jaeger, S. Fischer and O. V. Prezhdo, *J. Chem. Phys.*, 2012, **137**, 22A545.
55 W. Chu, Q. Zheng, O. V. Prezhdo, J. Zhao and W. A. Saidi, *Sci. Adv.*, 2020, **6**, eaaw7453.
56 W. Chu, W. A. Saidi, J. Zhao and O. V. Prezhdo, *Angew. Chem., Int. Ed.*, 2020, **59**, 6435–6441.
57 C. F. Craig, W. R. Duncan and O. V. Prezhdo, *Phys. Rev. Lett.*, 2005, **95**, 163001.
58 C. Zhang, Y. Shi, Y. Si, M. Liu, L. Guo, J. Zhao and O. V. Prezhdo, *Nano Lett.*, 2022, **22**, 6334–6341.
59 M. Kato, Y. Shichibu, K. Ogura, M. Iwasaki, M. Sugiuchi, K. Konishi and I. Yagi, *J. Phys. Chem. Lett.*, 2020, **11**, 7996–8001.
60 A. Wing-Bocanegra and A. Tlahuice-Flores, *Phys. Chem. Chem. Phys.*, 2019, **21**, 23855–23864.